# A Mechanistic Growth Model for Inorganic Crystals: Growth Mechanism

**Preshit Dandekar and Michael F. Doherty**
Dept. of Chemical Engineering, University of California Santa Barbara, Santa Barbara, California 93106-5080

*DOI 10.1002/aic.14513*
*Published online September 16, 2014 in Wiley Online Library (wileyonlinelibrary.com)*

*Inorganic crystals grown from solution find wide application. A mechanistic growth model based on the spiral growth mechanism that operates at low supersaturation on inorganic crystal surfaces is presented. The long-range electrostatic interactions on inorganic crystal surfaces are captured by methods developed in our previous article (Dandekar and Doherty, AIChE J., in press). The interactions of kink site growth units with the solvent molecules partially determine the growth kinetics. Relevant experimental parameters are systematically accounted for in the expression for the kink incorporation rate along step edges on the crystal surfaces. The growth model accurately predicts the asymmetric growth spirals on the* $(10\bar{1}4)$ *surface of calcite crystals. The effect of supersaturation and ionic activity ratio on the step velocities of the acute and obtuse spiral edges is also correctly captured. This model can be used to predict the shapes of solution grown inorganic crystals and to engineer the growth process to design inorganic solids with functionally desirable shapes.* © 2014 American Institute of Chemical Engineers *AIChE J*, 60: 3720–3731, 2014
*Keywords: spiral growth, inorganic crystallization, biomineralization, calcite growth, crystal morphology prediction*

## Introduction

In a previous article,[1] we proposed a mechanistic framework to model the solid-state interactions in inorganic crystals from a crystal growth and shape evolution point of view. Modeling surface integration-limited crystal growth from solution requires understanding the solid-state interactions as well as the surface growth mechanisms that govern the growth process. The importance of the interactions between the crystal and the solvent in modeling inorganic crystal growth from solution is highlighted by the comparable magnitudes of the lattice energy and the hydration energy for most inorganic solids (both energies have magnitudes typically $> 100$ kcal/mol). The lattice energy is dominated by the interionic long-range electrostatic interactions in the solid state, while the hydration energy depends on the interactions between the solvated ions and the water molecules present in the solvation shell. For example, the lattice dissociation enthalpy for cubic NaCl crystal is 188.1 kcal/mol[1] while the combined hydration enthalpy for $Na^+$ and $Cl^-$ions is $-187.2$ kcal/mol.[3,4] As a result, the dissolution enthalpy for NaCl crystal in aqueous solution is only 0.9 kcal/mol. Thus, the interactions of the surface growth units with the solvent play a huge role in determining the kinetics of the individual processes involved in growth on inorganic crystal surfaces.

Crystal growth of inorganic crystals, such as calcium carbonate, barium sulfate, potassium dihydrogen phosphate (KDP) and so forth, from solution has been well studied experimentally. The surface growth mechanisms, such as spiral growth and two-dimensional (2-D) nucleation, have been experimentally observed using surface characterization techniques such as atomic force microscopy (AFM).[5–9] The characterization of the crystal-solution interface, using techniques such as scanning tunneling microscopy, low-energy electron diffraction, X-ray reflectivity measurements and so forth, provides valuable information about the surface structure that is used along with the AFM measurements to elucidate the growth mechanism active on the crystal surface.[10] Crystal growth models for inorganic solids that have been developed so far can be divided into two categories—(1) those that study the solid-state interactions on a molecular scale and use the attachment energy model to predict the crystal growth rate and steady-state morphology[11–14] and (2) those that develop a mechanistic growth model but use experimentally fitted values for nearest-neighbor interactions.[15,16] A mechanistic crystal growth model that accounts for the solid-state electrostatic interactions as well as the solvent–solute interactions has not yet been developed for inorganic solids. Such a growth model will have predictive capability on a macroscopic scale to prescribe more efficient crystal growth experiments. The challenge here is to study both the solid-state interactions and the effect of the solvent on the growth kinetics in a generalized manner so that the conclusions from the model predictions can be applied to the crystal growth of any inorganic crystal surface. We make a distinction between growth on nonpolar crystal surfaces and polar crystal surfaces. The stabilization and growth mechanisms on polar inorganic crystal surfaces is not yet fully understood and will not be discussed here (The reader is referred to review articles on polarity of oxide crystal surfaces by Diebold et al.[17] and Goniakowski et al.[18]). The subject of this study

Additional Supporting Information may be found in the online version of this article.

Correspondence concerning this article should be addressed to M. F. Doherty at mfd@engineering.ucsb.edu.

is the growth mechanism active on nonpolar inorganic crystal surfaces that do not undergo heavy surface reconstruction to stabilize themselves.

In this work, we present a generalized methodology to study the spiral growth mechanism on inorganic crystal surfaces. The step velocities of spiral edges on an inorganic crystal surface can be calculated using the kink rate and kink density models discussed here. The density of kink sites along a spiral edge is calculated from the equilibrium distribution of disturbances due to thermal roughening.[19,20] The rate of kink propagation on an ionic step edge is calculated using detailed balances with appropriate expressions for the kink attachment and detachment fluxes that account for solution composition and kink site interaction energies. This mechanistic growth model is applied to the crystal growth on the $\{10\bar{1}4\}$ family of faces on calcite ($CaCO_3$) crystals. Calcite is the most stable and abundant polymorph of calcium carbonate and its crystal growth is well studied from a biomineralization perspective.[21] The surface growth mechanisms in presence of impurities such as $Mg^{2+}$, $Sr^{2+}$ and biomolecules that are typically present in the marine ecosystem are well studied experimentally.[22–26] Our model does well in predicting the shape of the growth spirals formed on calcite crystal surfaces but also the effect of the environmental composition on the step velocities of the spiral edges on the $(10\bar{1}4)$ calcite surface. The model can be applied to study crystal growth, shape evolution, and the steady-state shape achieved by typical inorganic salts grown from aqueous solution. We expect that the model can be used to design suitable zeolite growth modifiers that provide functionally desirable crystal morphology for various zeolite systems such as ZSM-5,[27] silicalite-1,[28] and zeolite L.[29,30]

## Growth Mechanism

Growth of crystal surfaces occurs under nonequilibrium conditions when the chemical potential of the growth medium ($\mu_m$) is greater than the chemical potential of the bulk crystal ($\mu_c$). The difference ($\Delta\mu$) between these chemical potentials is the driving force for crystal growth

$$\Delta\mu = \mu_m - \mu_c \tag{1}$$

When the rate of mass transfer between the bulk growth medium and the crystal surface is much faster than the rate of incorporation of the growth units into the crystal lattice, crystal surfaces grow by a layered growth mechanism. The crystal surface grows by the attachment of growth units along steps present on the surface. These steps may originate from either growth spirals or 2-D nuclei present on the surface. At low supersaturation, the activation energy for the formation of 2-D nuclei is very high, therefore, the growth rate is dominated by the spiral growth mechanism.[31,32] A crystal surface contains screw dislocations that act as the source of atomic steps, where growth units are preferentially incorporated into the crystal. These steps spread across the surface due to the attachment of growth units and result in a self-perpetuating growth of layers on top of other layers that gives rise to growth hillocks with a spiral pattern.[20,33] The perpendicular growth rate $G_{hkl,s}$ of a crystal face with Miller index $\{hkl\}$, growing by the spiral growth mechanism, is related to the rotation time $\tau_s$ of the growth spiral as follows[33]

$$G_{hkl,s} = \left(\frac{h}{\tau_s}\right)_{hkl} \tag{2}$$

$$\tau_s = \sum_{i=1}^{N} \frac{l_{c,i+1}\sin\left(\alpha_{i,i+1}\right)}{\mathrm{v}_i} \tag{3}$$

where $h$ is the height of the spiral edge, $N$ is the number of edges in the growth spiral, $l_{c,i}$ is the critical length of spiral edge $i$, $\alpha_{i,i+1}$ is the angle between edges $i$ and $i+1$, and $\mathrm{v}_i$ is the step velocity of edge $i$. One definition of the critical length $l_{c,i}$ of edge $i$ is the minimum length above which the free energy change associated with the addition of a new row of growth units along the edge $i$ is negative.[33] Since a spiral edge moves by the incorporation of growth units into the kink sites present along the edge, the growth kinetics of the crystal surface depends on the rate of attachment of growth units into kink sites.

The step velocity of each spiral edge on every surface of the crystal must be calculated to predict the growth rates and, therefore, the steady-state crystal morphology. The step velocity $\mathrm{v}_i$ of a spiral edge $i$ is written as follows[15,34]

$$\mathrm{v}_i = a_{p,i}\rho_i u_i \tag{4}$$

where $a_{p,i}$ is the perpendicular distance between two rows of the spiral edge $i$ (units of Å or nm), $\rho_i$ is the density of kink sites along the edge $i$ (dimensionless) and $u_i$ is the net rate of attachment of growth units into the kink sites (units of $s^{-1}$). $a_p$ depends on the crystallography and step structure while the kink density is given by the thermodynamics of creating kink sites from a straight step edge.[20] Kink rate $u$ captures the kinetics of the crystal growth process and combines the rates of the competing processes of attachment and detachment of growth units into and from the kink sites, respectively. The density of kink sites along an edge and the net rate of incorporation into the kink sites depend on the interaction energies of growth units along the edge. Therefore, the first step in crystal growth modeling is the identification of the Periodic Bond Chain (PBC) directions that are parallel to the strongest intermolecular interactions between the growth units in the solid state. A systematic method to identify the PBC directions in inorganic crystals has been presented earlier.[1] The interaction energies of growth units present along the spiral edges are calculated while including the surface effect on the partial charges of growth units and the long-range electrostatic interactions.[1] A general method that uses those interaction energies to calculate the kink density and the kink rate for inorganic crystal growth is presented in the following sections.

## Kink Density Calculation

The edges on a crystal surface undergo constant thermal fluctuation and are never completely straight at any temperature $T > 0$ K.[20] These thermal fluctuations provide a finite density of kink sites along the edge where growth units attach. The density of these kink sites or the spacing between two successive kink sites along the edge partially determines the net rate at which the step edge moves due to attachment of growth units (see Eq. 4).

Using the statistical mechanics of fluctuations, Frenkel[19] and Burton et al.[20] developed a method to calculate the density of kink sites along an edge. The probability of finding a kink site along the edge depends on the energy required to

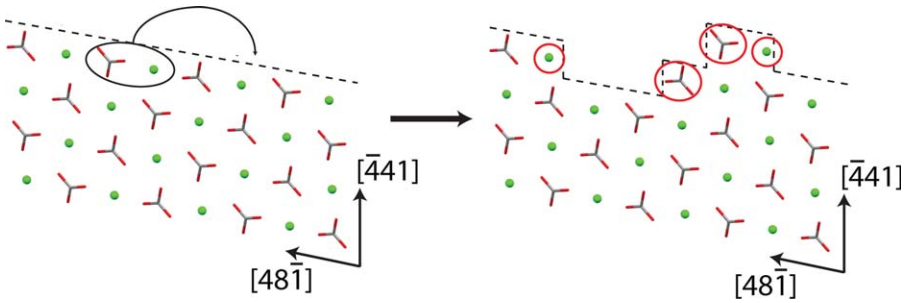


**Figure 1. A representative rearrangement of a Ca and a $CO_3$ growth unit (within the black circle) from a straight [48$\bar{1}$] edge on (10$\bar{1}$4) surface of calcite to form four kink sites (red circles).**

**The water molecules surrounding the edge and kink sites have not been shown. [Color figure can be viewed in the online issue, which is available at wileyonlinelibrary.com.]**

rearrange two adjacent growth units from a straight edge to form an edge with four kink sites.[20] If the energy required per kink site for this rearrangement, called the kink energy, is of the order of thermal energy ($k_BT$), the rearrangement occurs on a time scale faster than the attachment/detachment of growth units into the kink sites.[35] Therefore, the edge structure is always in quasi-equilibrium with respect to the growth medium and the kink sites are Boltzmann distributed.

Kuvadia and Doherty proposed a systematic method to calculate the kink density on step edges with multiple types of kink sites on organic crystal surfaces.[34] The probability of observing any type of kink site can be computed by counting all the microstates of edge rearrangements that expose that particular kink type and by calculating the energy for each rearrangement.

The probability of observing any particular rearrangement depends on the change in the potential energy of the system on the rearrangement of the edge. Therefore, the calculation of kink density on the step edges on an inorganic crystal surface involves computing the change in potential energy of the entire system due to a rearrangement of a straight edge. The system consists of a step edge on a crystal surface as well as the solvent molecules in the immediate vicinity of the step edge. The rearrangement of two adjacent growth units along a straight edge to a step adatom position (Figure 1) involves the breaking of solid–solid "bonds" as well as formation of new solid–solvent "bonds." The new solid–solvent interactions are formed because the solvent structure around an edge growth unit is different from that around a growth unit in a kink site.[36] The change in the potential energy of the entire system due to this rearrangement must reflect the changes in both solid–solid and solid–solvent interactions.

The kink densities on the spiral edges of the (10$\bar{1}$4) surface of calcite were calculated using this method. As discussed previously, there are two spiral edges— [$\bar{4}$41] and [48$\bar{1}$] on the (10$\bar{1}$4) surface of calcite.[1] Each of these two edges has obtuse and acute orientations depending on the angle that the step edge makes with the plane of the crystal surface. We have shown previously that either of the orientations on both [$\bar{4}$41] and [48$\bar{1}$] edges are symmetrically equivalent,[1] so we only discuss the [48$\bar{1}$] edge henceforth (Figure 1).

The [48$\bar{1}$] edge has four growth units that repeat along the edge—two calcium and two carbonate ions. The two carbonate growth units differ in their orientations, therefore, the two calcium growth units situated between them have different interaction energies. When considering the rearrangement of a straight [48$\bar{1}$] edge, there are four choices to select a pair of adjacent growth units along the edge to be moved. Similarly, there are four choices for the final positions of the earlier selected pair of growth units as step adatoms. Therefore, there are 16 possible rearrangements on each obtuse and acute orientation of the [48$\bar{1}$] edge. Also, each of the kink sites on the edge can have two possible orientations— $\mathscr{E}$ and $\mathscr{W}$. The $\mathscr{E}$ and $\mathscr{W}$ orientations of the kink sites correspond to the kink site growth unit facing east and west, respectively, when the edge grows in the north direction (Figure 2). Therefore, there are a total of eight kink sites on the [48$\bar{1}$] edge on (10$\bar{1}$4) surface of calcite.

Table 1 shows the kink densities of all the kink sites on both [48$\bar{1}$] acute and [48$\bar{1}$] obtuse edges. The total density of kink sites is higher on the acute edge than the obtuse edge. As the step velocity is directly proportional to the kink density along the edge, the difference in kink densities between the obtuse and acute spiral edges on the (10$\bar{1}$4) surface of calcite does explain the asymmetry in the shape of the growth spirals found on the crystal surface. However, the net rate of attachment into the kink sites must also be calculated before predicting the step velocities and the exact shape of the growth spirals.

## Kink Rate for Inorganic Crystals

The net rate of attachment or detachment of growth units from kink sites along a step edge on a crystal surface is called the rate of kink incorporation or the kink rate.[37] Kink rate models have been developed for both organic molecular crystals[34] and ionic crystals.[15] However, these models were limited in their scope of the solid-state interactions and considered only nearest-neighbor interactions. The kinetics of attachment/detachment of ionic growth units will depend on the potential energies of the ions in the kink sites. In our previous article, we have successfully developed a systematic method to calculate the kink site potential energies of ions accounting for both long-range solid-state interactions as well as the solid-solvent interactions.[1]

The kink rate model developed by Zhang and Nancollas[15] is applicable for two types of kink sites along a step edge on the surface of an AB-type ionic crystal. Frequently, the step edges on inorganic crystal surfaces may have different orientations or positions for both cations and anions that result in more than two types of kink sites along a step edge. Therefore, a general kink rate model for inorganic crystals is

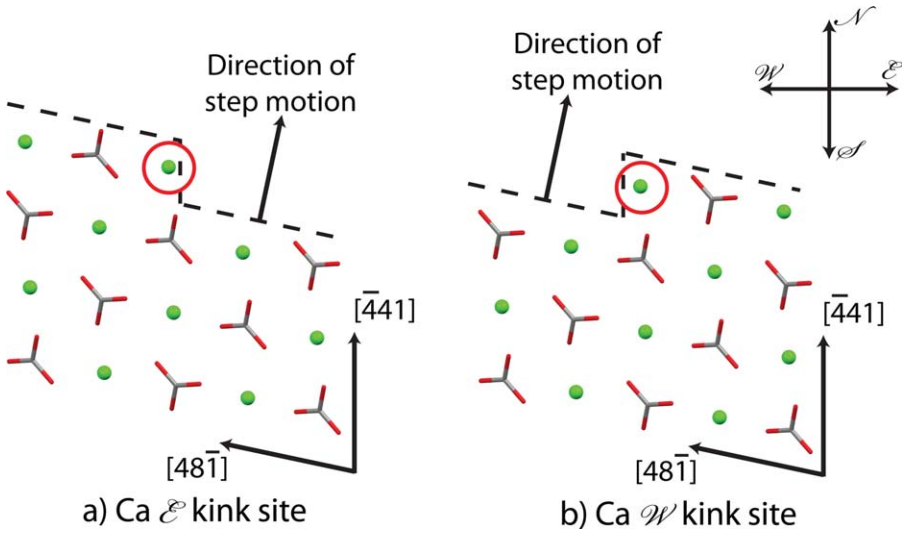


**Figure 2. The two orientations ($\mathscr{E}$ and $\mathscr{W}$) of kink sites on the [48$\bar{1}$] edge on ($10\bar{1}4$) surface of calcite.**

**[Color figure can be viewed in the online issue, which is available at wileyonlinelibrary.com.]**

required that allows for multiple types of kink sites present along the edge.

### *New kink rate model*

Kuvadia and Doherty[34] developed a generalized expression for the kink rate $u$ on a spiral edge on organic crystal surfaces that has $n$ types of kink sites along the edge

$$u=\frac{(j^+)^n-\prod_{k=1}^{n} j_k^-}{\sum_{\ell=1}^{n}(j^+)^{n-\ell}(j^-)^{(\ell-1)}} \tag{5}$$

where $j^+$ is the attachment flux of growth units into the kink site and $j_k^-$ is the detachment flux from the kink site $k$. $j^+$ is independent of the specific kink site and depends only on supersaturation and solution composition, whereas $j_k^-$ depends on the solution chemistry and the local bonding energies for the kink site $k$.[35,38,39] The quantity $(j^-)^{(\ell-1)}$ in Eq. 5 is given by

$$(j^-)^{(\ell-1)}=\sum_{k=1}^{n} j_k^- j_{k+1}^- j_{k+2}^- \cdots j_{k+\ell-2}^- \tag{6}$$

Equation 5 holds true for molecular crystals, where all the growth units are a single chemical species so that the solvation behavior is the same for all of them. In case of inorganic crystal growth, the growth units are ions (positive and negative) and will exhibit different solvation behavior and attachment kinetics.

Figure 3 shows a representative arrangement of multiple types of kink sites along a step edge on the surface of an AB-type ionic crystal where each ion has two distinct orientations. The attachment of a B growth unit into an A-terminated kink site results in the exposure of a B-terminated kink site. Similarly, the detachment from an A-terminated kink site results in the exposure of another B-terminated kink site.

It is assumed that the edge begins with an A-type kink site and alternates between an A-type and a B-type kink site. Therefore, the odd and even numbered kink sites will be terminated by cationic (A) and anionic (B) species, respectively. If there are $N$ orientations each of cationic and anionic growth units along the edge, there will be a total of $2N$ types of kink sites on the edge. $P_{2k-1}$ and $P_{2k}$ are defined as the probabilities that the step edge is terminated with an A kink site and a B kink site of type $(2k-1)$ and $2k$, respectively. Therefore, $k$ takes all the integer values between 1 and $N$. We define the edge to be in state $2k-1$ if it is terminated with the kink site numbered $2k-1$. The transition between any two successive states or types of kink sites is associated with attachment ($j^+$) or detachment ($j^-$) fluxes. Figure 4 shows the transition between the $2k-1$, $2k$, and $2k+1$ states of the kink site. It is well accepted[35,38,39] that the attachment flux $j^+$ depends on the solvation chemistry of the attaching growth unit and the solution composition but is independent of the kink site location along the edge. The detachment flux $j^-$depends on both solution chemistry and the local bonding energies at the kink site location along the edge.

The kink incorporation rate on the step edge is given by the net rate at which the edge transitions from one state to the next. At steady state, the net rate of incorporation is exactly equal for each state or kink type. Therefore, the kink rate $u$ for states $2k-1$ and $2k$ is given by

$$u_{2k-1}=j_B^+P_{2k-1}-j_{2k}^-P_{2k} \quad u_{2k}=j_A^+P_{2k}-j_{2k+1}^-P_{2k+1} \tag{7}$$

The probability $P_{2k}$ of a state $2k$ is calculated by setting up a steady-state balance for the influx and outflux into and

**Table 1. Density of Kink Sites on the [48$\bar{1}$] Spiral Edges of ($10\bar{1}4$) Face of Calcite**

| | | Kink Density $\rho$ | |
|---|---|---|---|
| Edge Type | Growth Unit | $\mathscr{E}$ | $\mathscr{W}$ |
| [48$\bar{1}$] Obtuse | Ca (1) | 0.0021 | 0.0136 |
| | $CO_3$ (1) | 0.0065 | 0.0021 |
| | Ca (2) | 0.0021 | 0.0065 |
| | $CO_3$ (2) | 0.0136 | 0.0021 |
| | Total | 0.0243 | 0.0243 |
| [48$\bar{1}$] Acute | Ca (1) | 0.0139 | 0.0092 |
| | $CO_3$ (1) | 0.005 | 0.0139 |
| | Ca (2) | 0.004 | 0.005 |
| | $CO_3$ (2) | 0.0092 | 0.004 |
| | Total | 0.0321 | 0.0321 |

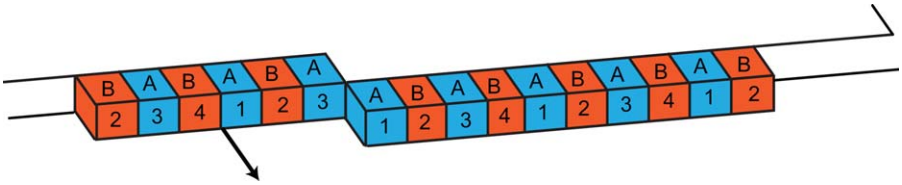


**Figure 3. A representative arrangement of multiple types of kink sites along the edge of an AB-type ionic crystal surface.**

**There are two types of A (cyan) and B (orange) kink sites each that are repeated by symmetry along the edge. The arrow indicates the direction of the growth of the step. [Color figure can be viewed in the online issue, which is available at wileyonlinelibrary.com.]**

out of state $2k$, respectively. The detailed balance master equation is written as follows

$$j_B^+ P_{2k-1} + j_{2k+1}^- P_{2k+1} = \left(j_A^+ + j_{2k}^-\right) P_{2k} \tag{8}$$

Similar equations can be written for each type of kink site giving rise of $2N$ such equations. However, due to the cyclic repetition of the arrangement of the kink sites beyond state $2N$, there are only $2N-1$ independent equations. The condition that the kink state probabilities $P_k$ must all sum up to 1 provides the $2N$th equation to solve for all the probabilities in terms of the attachment and detachment fluxes. The kink rate $u$ can thus be calculated as follows

$$u = \frac{\left(j_A^+ j_B^+\right)^N - \prod_{k=1}^{2N} j_k^-}{\sum_{\ell=1}^{N} \left(j_A^+ j_B^+\right)^{N-\ell} \left\{ \left(j^-\right)^{(2\ell-1)} + j_A^+ \left(j_{\text{even}}^-\right)^{(2\ell-2)} + j_B^+ \left(j_{\text{odd}}^-\right)^{(2\ell-2)} \right\}} \tag{9}$$

where

$$\left(j_{\text{odd}}^-\right)^{(\ell)} = \sum_{k=1}^{N} j_{2k-1}^- j_{2k}^- j_{2k+1}^- \cdots j_{2k+\ell-2}^-$$

$$\left(j_{\text{even}}^-\right)^{(\ell)} = \sum_{k=1}^{N} j_{2k}^- j_{2k+1}^- j_{2k+2}^- \cdots j_{2k+\ell-1}^-$$

$$\left(j^-\right)^{(\ell)} = \sum_{k=1}^{2N} j_k^- j_{k+1}^- j_{k+2}^- \cdots j_{k+\ell-1}^- = \left(j_{\text{odd}}^-\right)^{(\ell)} + \left(j_{\text{even}}^-\right)^{(\ell)}$$

Equation 9 can be used to calculate the kink rate $u$ on any edge on any crystal surface, provided the attachment and detachment fluxes ($j^+$ and $j^-$, respectively) from kink sites are known. General expressions for these fluxes and a systematic method for their calculation are discussed next.

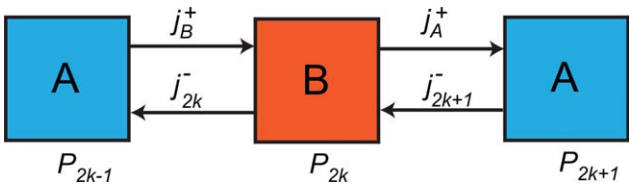


**Figure 4. Transitions between A and B kink sites based on the attachment or detachment of A and B growth units and the fluxes associated with these transitions.**

**[Color figure can be viewed in the online issue, which is available at wileyonlinelibrary.com.]**

### *Expressions for attachment and detachment fluxes*

We use transition state theory (TST)[40] to calculate the kink site attachment and detachment fluxes. The reaction coordinate is assumed to be the distance from the kink site towards the solution so that the reactant state corresponds to the growth unit docked in its kink site and the product state corresponds to the growth unit fully solvated in bulk solution (Figure 5). The transition state corresponds to a partially broken solvation shell that is also partially bonded to its neighbors around the kink site. In this case, the attachment and detachment fluxes depend on the reverse and forward "reaction rates," respectively, as shown in Eqs. 10 and 11.

A generalized model for the attachment and detachment fluxes must account for the presence of both cationic and anionic growth units in the solution. Additives, impurities, counterions and antisolvents may also be present in the solution. These foreign species can be classified into three groups—(I) species that can incorporate into the crystal lattice (e.g., chemically similar additives or modifiers such as $Mg^{2+}$ ions in calcite), (II) species that influence detachment of growth units from kink sites (e.g., antisolvent), and (III) species that do not participate in any of the steps associated with attachment or detachment of growth units into kink sites (e.g., counterions). The mole fractions of these three types of species in the solution are $x_{\text{I}}$, $x_{\text{II}}$, and $x_{\text{III}}$, respectively.

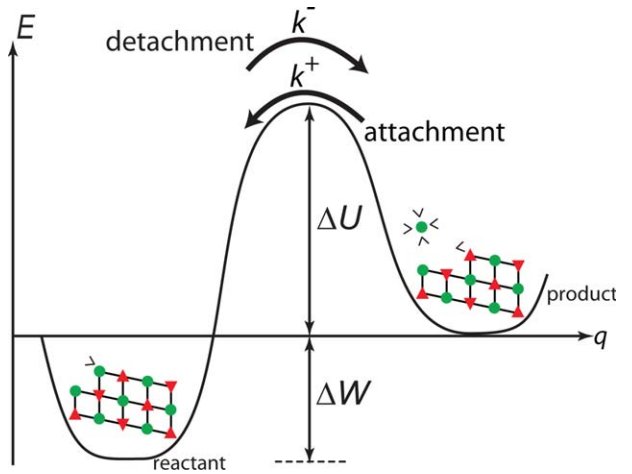


**Figure 5. Representative energy landscape during attachment and detachment from kink sites.**

**The reactant state is the growth unit attached in the kink site. The product state is the unattached kink site and fully solvated growth unit in the solution. $k^+$ and $k^-$ are the rate constants for the attachment and detachment processes, respectively. [Color figure can be viewed in the online issue, which is available at wileyonlinelibrary.com.]**

The prefactor for the TST rate constant contains partition functions for the solvated growth unit and for the kink site on the crystal surface. The prefactor value will be different for cationic and anionic growth units. The attachment flux of an ionic species into a kink site is proportional to its mole fraction in the adsorption layer.[38] If the bulk transport rate is much faster than the rate of surface integration, the mole fraction of solute molecules in the adsorption layer next to the crystal surface will be the same as the bulk solution mole fraction. Therefore, the attachment flux $j^+$ for both the ions is written as

$$j_A^+ = \nu_A \exp\left(-\frac{\Delta U_A}{k_B T}\right) x_A = k_A^+ x_A$$
$$j_B^+ = \nu_B \exp\left(-\frac{\Delta U_B}{k_B T}\right) x_B = k_B^+ x_B \tag{10}$$

where $\nu_A$ and $\nu_B$ are the vibrational frequencies of attachment and detachment attempts that depend on the temperature and the partition functions of the solute, solvent, and the transition state solvated complex. These frequencies are assumed to be the same everywhere on the crystal surface. The attachment energy barriers correspond to the breaking of the solvation shell around the growth units so the barrier heights $\Delta U_A$ and $\Delta U_B$ will be constant on all crystal faces. $x_A$ and $x_B$ are the respective mole fractions of the cationic and anionic growth units in the solution. $k_A^+$ and $k_B^+$ are the first-order rate constants for attachment of A and B ions, respectively, into kink sites.

The detachment flux for both types of growth units is proportional to the combined mole fraction of solvent molecules and species of type II in the adsorption layer.[38] The detachment flux $j^-$ for each of the kink sites is given by

$$j_{2k-1}^- = (1 - x_A - x_B - x_I - x_{III})\nu_A \exp\left(-\frac{\Delta U_A + \Delta W_{2k-1}}{k_B T}\right)$$
$$j_{2k}^- = (1 - x_A - x_B - x_I - x_{III})\nu_B \exp\left(-\frac{\Delta U_B + \Delta W_{2k}}{k_B T}\right) \quad k = 1, 2, 3 \ldots, N \tag{11}$$

where $\Delta W_{2k-1}$ is the work required to remove the partially solvated growth unit from the $2k-1$ kink site position to a fully solvated state in the bulk solution. $\Delta W_{2k-1}$ depends on the interactions between the growth unit which is docked in the $2k-1$ kink site and the crystal as well as its interactions with the solvent. For vapor grown crystals, $\Delta W_{2k-1}$ will be given by the sum of the solid broken bond energies at kink site $2k-1$. As discussed earlier, $j_{2k-1}^-$ and $j_{2k}^-$ are the detachment fluxes for the $2k-1$ (cationic) and $2k$ (anionic) kink sites, respectively. The expressions for the attachment and detachment fluxes from Eqs. 10 and 11, respectively, can be put into Eq. 9 to calculate the kink propagation rate at any step edge on an inorganic crystal surface. It is convenient to express the mole fractions of A and B ions in the solution ($x_A$ and $x_B$, respectively) in terms of two experimental parameters—supersaturation $S$, and ionic activity ratio $r$.

Supersaturation or saturation ratio $S$ of the aqueous solution of a general electrolyte $A_\alpha B_\beta$ is defined in terms of the difference between the chemical potentials of the solution phase and the crystal as follows[15,41,42]

$$\Delta\mu = (\alpha + \beta) k_B T \ln S = k_B T \ln\left(\frac{a_A^\alpha a_B^\beta}{K_{sp}}\right) \tag{12}$$

where $K_{sp}$ is the solubility product of $A_\alpha B_\beta$ salt. For an AB type salt, the supersaturation $S$ is defined as

$$S = \left(\frac{a_A a_B}{K_{sp}}\right)^{1/2} = \left(\frac{(M\gamma_A x_A)(M\gamma_B x_B)}{K_{sp}}\right)^{1/2} = \left(\frac{\gamma_A \gamma_B x_A x_B}{K_{sp}/M^2}\right)^{1/2} \tag{13}$$

where $\gamma_A$ and $\gamma_B$ are the activity coefficients and $M$ is the molarity of the solution. For dilute aqueous solutions, $M = 55.56$ mol $L^{-1}$. Relationships between $S$ and other measures of supersaturation are described in Appendix B. The ionic activity ratio $r$ is defined as

$$r = \frac{a_A}{a_B} = \frac{\gamma_A x_A}{\gamma_B x_B} \tag{14}$$

The relationship between the mole fractions ($x_A$ and $x_B$), supersaturation $S$, and activity ratio $r$ (from Eqs. 13 and 14) is

$$x_A = \frac{S\sqrt{r}}{\gamma_A}\left(\frac{\sqrt{K_{sp}}}{M}\right) \quad x_B = \frac{S}{\gamma_B\sqrt{r}}\left(\frac{\sqrt{K_{sp}}}{M}\right) \tag{15}$$

These two experimental parameters ($S$ and $r$) can be independently manipulated during the crystallization process. The more common experimental cases are when either the supersaturation[43] or the ionic activity ratio is constant.[44]

The condition of thermodynamic equilibrium provides a relationship between the attachment and detachment fluxes. At equilibrium, the step velocity is zero so the kink rate must be zero. It follows from Eq. 9 that at equilibrium

$$\left(j_{A,eq}^+ j_{B,eq}^+\right)^N = \prod_{k=1}^{2N} j_{k,eq}^- \tag{16}$$

The equilibrium attachment and detachment fluxes are obtained by replacing $x_A$ and $x_B$ in Eqs. 10 and 11 by $x_{A,eq}$ and $x_{B,eq}$, respectively. The expressions for $j_{eq}^+$ and $j_{eq}^-$ are substituted into Eq. 16, which results in

$$-\frac{1}{2N}\sum_{k=1}^{2N}\left(\frac{\Delta W_k}{k_B T}\right) = \ln\left(\frac{\sqrt{x_{A,eq}\, x_{B,eq}}}{1 - x_{A,eq} - x_{B,eq} - x_I - x_{III}}\right) \tag{17}$$

The left-hand side of Eq. 17 contains quantities that are calculated from the intermolecular interactions while the right-hand side contains quantities whose values are experimentally obtained. Therefore, this equation can be used as a consistency check to verify the calculations of the solid-state and solvent interaction energies, so that the calculated values of $\Delta W_k$ from the model are consistent with the equilibrium mole fractions calculated from the experimentally obtained value of the solubility product $K_{sp}$ (by putting $S = 1$ in Eq. 15). If the two sides of Eq. 17 do not match, a local solubility product $K_{sp}'$ near the crystal surface can be calculated from the $\Delta W_k$ values as follows

$$K_{sp}' = \frac{\gamma_A \gamma_B M^2 (1 - x_I - x_{III})^2 \exp\left\{-\frac{1}{N}\sum_{k=1}^{2N}\left(\frac{\Delta W_k}{k_B T}\right)\right\}}{\left[1 + \left(\frac{1 + r_{eq}\gamma_B/\gamma_A}{\sqrt{r_{eq}\gamma_B/\gamma_A}}\right)\exp\left\{-\frac{1}{2N}\sum_{k=1}^{2N}\left(\frac{\Delta W_k}{k_B T}\right)\right\}\right]^2} \tag{18}$$

where $r_{eq}$ is the value of the ionic activity ratio at equilibrium. If the crystallization process occurs at constant ionic activity ratio, $r_{eq} = r$ and Eq. 18 can be used to calculate the local solubility product and hence the equilibrium mole fractions of A and B (from Eq. 15). However, if the crystallization process occurs at variable $r$, $r_{eq}$ may be different from the variable values of $r$. In that case, Eq. 18 can be solved

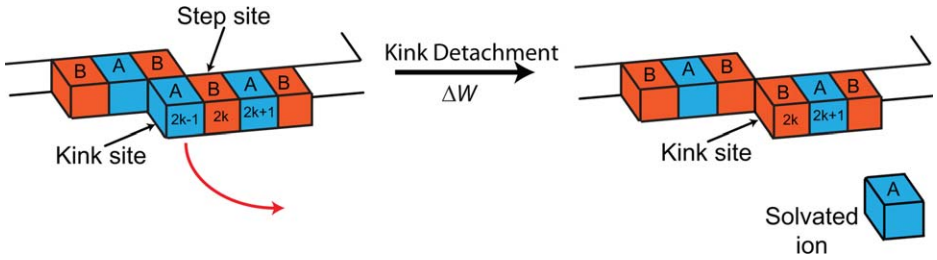


**Figure 6. Illustration of the detachment process of an A-type kink site that results in the formation of a B-type kink site.**

**The change in the potential energy of the system in this process is given by the kink detachment work $\Delta W$. The solvent molecules around the edge are not shown for clarity. [Color figure can be viewed in the online issue, which is available at wileyonlinelibrary.com.]**

only if the equilibrium mole fractions of A and B are very small ($x_{A,\mathrm{eq}}, x_{B,\mathrm{eq}} \ll 1$). Equation 18 is then simplified as follows

$$K_{\mathrm{sp}}^{'} = \gamma_A \gamma_B M^2 (1 - x_{\mathrm{I}} - x_{\mathrm{III}})^2 \exp\left\{ -\frac{1}{N} \sum_{k=1}^{2N} \left( \frac{\Delta W_k}{k_{\mathrm{B}} T} \right) \right\} \quad (19)$$

The solubility of several inorganic crystals, such as calcite, barite, rutile and KDP, in water is very low.[2,45] Therefore, the assumption that $x_{A,\mathrm{eq}}, x_{B,\mathrm{eq}} \ll 1$ is quite reasonable for these crystals. For the sake of internal consistency, the value of $K_{\mathrm{sp}}^{'}$ from Eq. 19 is used instead of the experimental value ($K_{\mathrm{sp}}$) in the subsequent equations. The mole fractions of A and B in the supersaturated solution ($x_A$ and $x_B$) are thus calculated by substituting $K_{\mathrm{sp}}$ with $K_{\mathrm{sp}}^{'}$ in Eq. 15. The activity coefficients $\gamma_A$ and $\gamma_B$ are calculated using Davies equation[46] that extends the Debye–Hückel theory to high concentration electrolyte solutions. If the mole fraction of the counterions present in the solution ($x_{\mathrm{III}}$) is much higher than $x_A$ and $x_B$, the activity coefficients are constant between the saturated and supersaturated solution and do not depend on $x_A$ and $x_B$.

The attachment and detachment fluxes are written in terms of the supersaturation $S$, ionic activity ratio $r$ and the local solubility product $K_{\mathrm{sp}}^{'}$ from Eqs. 10 and 11. The calculation of the kink rate $u$ from Eq. 9 requires that kink detachment work $\Delta W$ values be known. The detailed expressions for $j^+$, $j^-$ and $u$ as functions of $S$, $r$, and $\Delta W$ are given in Appendix A.

The kink site potential energies calculated in a previous article[1] are used to calculate the kink detachment work $\Delta W$. The species involved in the detachment process are—the growth unit about to be detached, the growth unit that forms the next kink site along the edge, and the solvent molecules that solvate both these growth units. Therefore, calculation of $\Delta W$ involves computing the kink site energies of the two successive growth units along the edge (Figure 6). The information on solvent structure around the kink site is used along with the space partitioning method to calculate the partial charges on the surface ions and the potential energy of a growth unit in the kink site.[1] Knowledge of the structure of the solvent shell around a growth unit in bulk solution, including the number of solvent molecules in the shell and their distances from the growth unit, is required to calculate the potential energy of the fully solvated growth unit. The solvation information of $Ca^{2+}$ and $CO_3^{2-}$ ions for calcite crystal growth was obtained from molecular simulations.[36,47,48] The expression for $\Delta W$ in terms of the kink site potential energy $U^{\mathrm{kink}}$ and potential energy of solvated ion $U^{\mathrm{solvated}}$ is given as follows

$$\Delta W_{2k-1} = U_A^{\mathrm{solvated}} + U_{2k}^{\mathrm{kink}} - U_{2k-1}^{\mathrm{kink}} - U_{2k}^{\mathrm{step}} \quad (20)$$

$$\Delta W_{2k} = U_B^{\mathrm{solvated}} + U_{2k+1}^{\mathrm{kink}} - U_{2k}^{\mathrm{kink}} - U_{2k+1}^{\mathrm{step}} \quad (21)$$

where $U^{\mathrm{step}}$ is the potential energy of an ion present along the step edge next to the kink site growth unit. $U^{\mathrm{step}}$ is calculated using the space partitioning method[1] with the partial charges for the atoms in the growth unit corresponding to that for a growth unit situated along the step edge. Figure 6 illustrates the kink detachment process and the change in the configuration of a B growth unit that lies next to the A-type

**Table 2. Kink Detachment Work ($\Delta W$) Values for the Kink sites on the [48$\bar{1}$] Spiral Edges of (10$\bar{1}$4) Face of Calcite**

| | | $\Delta W$ (kcal/mol) | |
|---|---|---|---|
| Edge Type | Growth Unit | $\mathscr{E}$ | $\mathscr{W}$ |
| [48$\bar{1}$] Obtuse | Ca (1) | 28.8 | 18.9 |
| | $CO_3$ (1) | 24.6 | 36.6 |
| | Ca (2) | 29.2 | 21 |
| | $CO_3$ (2) | 26.1 | 37.9 |
| [48$\bar{1}$] Acute | Ca (1) | 21.7 | 10.9 |
| | $CO_3$ (1) | 37.9 | 38.3 |
| | Ca (2) | 18.6 | 28.1 |
| | $CO_3$ (2) | 36.5 | 37.5 |

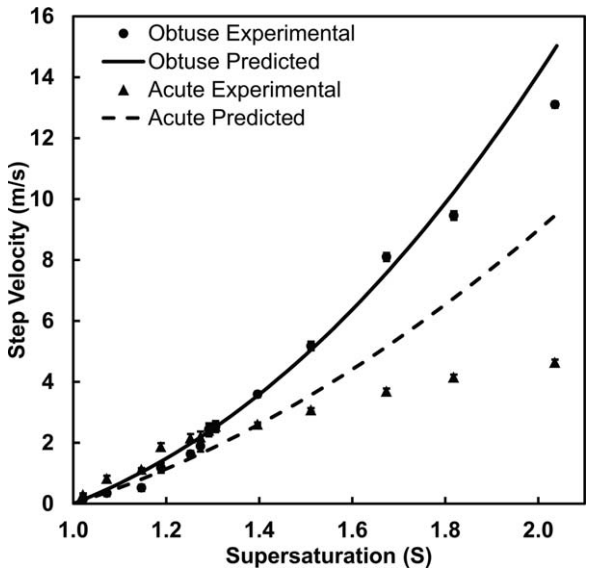


**Figure 7. Comparison of model predictions of the step velocities of obtuse and acute spiral edges with AFM measurements reported by Teng et al.[52] at $r = 1.04$.**

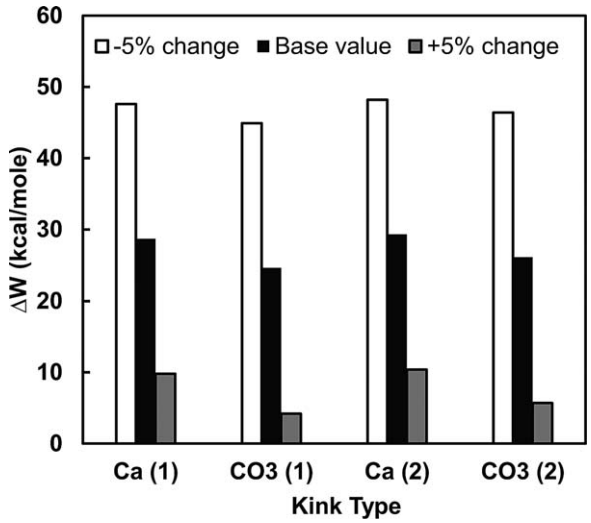


**Figure 8. Sensitivity of the kink detachment work $\Delta W$ to variations ($\pm 5\%$) in the interaction energies between the kink site ions and the surrounding water molecules for the kink sites with $\mathscr{E}$ orientation on the [$\bar{4}41$] obtuse edge on the $(10\bar{1}4)$ surface of calcite.**

kink site along the step edge and forms the new kink site (B type) after detachment of the A growth unit.

Table 2 shows the values of the kink detachment work ($\Delta W$) for the kink sites on the $[48\bar{1}]$ spiral edges (acute and obtuse) on a calcite $(10\bar{1}4)$ surface. As aforementioned, the $\Delta W$ values are the same for the kink sites on the symmetrically equivalent edges along the $[\bar{4}41]$ direction.

The $\Delta W$ values differ between the same type of kink sites on the obtuse and acute spiral edges. From Eq. 26 (Appendix A), it is evident that the kink rate, and thus the step velocity, should be different for the obtuse and acute edges on the $(10\bar{1}4)$ surface of calcite crystals. The model calculates the kink rate to within a multiplicative constant $k_A^+$, which is uniform on all crystal surfaces. Therefore, the absolute value of the step velocity of a spiral edge cannot be predicted without using molecular simulations with rare event methods[47,49] to estimate the value of $k_A^+$.

## Step Velocity Predictions on Calcite $(10\bar{1}4)$ Surface

The step velocity of spiral edges can be measured experimentally using AFM. The step velocity of spiral edges on a $(10\bar{1}4)$ surface of calcite have been measured using *in situ* AFM under various experimental conditions.[6,43,44,50,51] De Yoreo and coworkers[8,44,52] measured the step velocities of the spiral edges for a wide range of supersaturation ($1.02 < S < 2.04$), while keeping the ionic activity ratio constant at $r = 1.04$ (Appendix B provides expressions that relate the experimental measure of supersaturation to the value of $S$ used in this article). Figure 7 shows the comparison between the experimentally measured step velocities reported by Teng et al.[52] and predicted values from our model. The predicted step velocities were calculated assuming that no foreign species were present in the solution. The calculated values of step velocities were scaled with the experimental values at $S = 1.40$.

The model predictions for the step velocity of the obtuse edge match very well with the experimentally measured values except for very high supersaturation ($S \geq 1.8$). The predictions of our spiral growth model are not reliable at such high supersaturation, where growth by 2D nucleation was also observed in the AFM experiments.[44]

Step velocity predictions of the acute edge do not capture the supersaturation trend of the experimental measurements. Teng et al. observed a crossover between the step velocities of obtuse and acute edges at $S = 1.29$.[52] This crossover was explained by the effect of ppm level impurities (e.g., Mg, $SO_4$) present in the experimental reagents, on growth kinetics at the acute edge. These impurities adsorb on the terrace of the crystal surface and slow down the advancing steps, thereby changing the dependence of the step velocity on the supersaturation.[53] Teng et al.[52] showed that a sublinear dependence of the step velocity on the supersaturation fit the experimental data for the acute edge. Impurities such as $Mg^{2+}$ ions preferentially adsorb on the acute edges rather than the obtuse edges of $(10\bar{1}4)$ calcite surface.[54] Therefore, these ppm level impurities may have affected the step velocity measurement of the acute edges only. Our calculations do not account for the presence of any impurities in the solution or on the terrace. Therefore, we do not expect the supersaturation trend for the predicted step velocity of the acute edge to match with the experimental values.

The model does predict asymmetric growth spirals on the $(10\bar{1}4)$ surface of calcite and a higher step velocity of the obtuse edge than that of the acute edge at close to stoichiometric values of ionic activity ratio, which is consistent with other AFM measurements reported in the literature.[6,43]

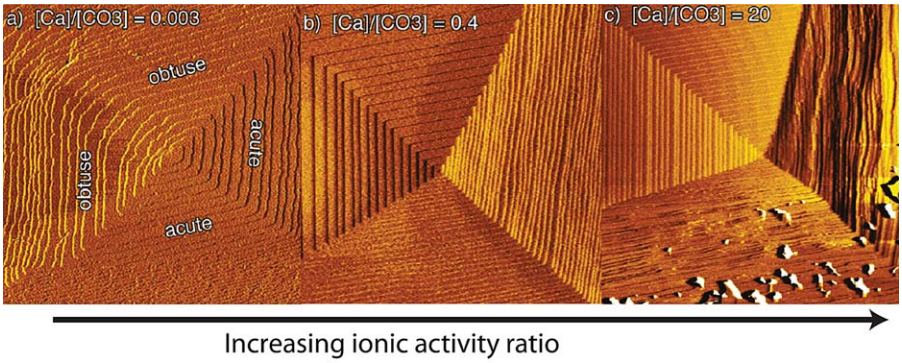


**Figure 9. *In situ* AFM images of growth spirals on the $(10\bar{1}4)$ surface of calcite crystal.**

**The activity ratio of $Ca^{2+}$ to $CO_3^{2-}$ ions increases from panels (a) to (c). Adapted from Ref 43, with permission from Copyright © 2010, American Chemical Society. [Color figure can be viewed in the online issue, which is available at wileyonlinelibrary.com.]**

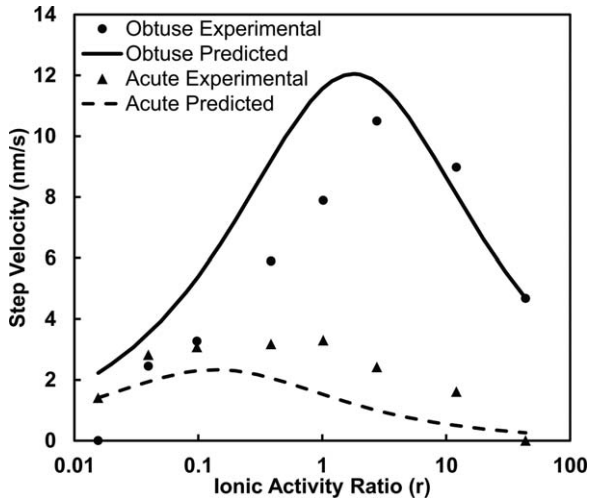


**Figure 10. Comparison of the variation of the step velocities of obtuse and acute spiral edges with increasing activity ratio of $Ca^{2+}$ to $CO_3^{2-}$ measured by Stack and Grantham[43] with the model predictions.**

**The experiments and the model predictions are at a constant supersaturation of $S = 1.58$.**

The values of the kink detachment work depend strongly on the interaction energies of the kink site ions with the solvent molecules. Figure 8 shows the change in the kink detachment work $\Delta W$ values for the $\mathscr{E}$ orientation kink sites on the $[48\bar{1}]$ obtuse edge as the interaction energies between water molecules and the $Ca^{2+}$ and $CO_3^{2-}$ ions and the water molecules is varied by 5%. The $\Delta W$ values change by at least $\pm 65\%$ due to a $\mp 5\%$ change in the interaction energy between the solvent molecules and the kink site ions (An increase in solvent interaction energy reduces the $\Delta W$ value). The change in the $\Delta W$ values is consistent for all the kink sites on obtuse and acute edges, therefore, the scaled values of the step velocity do not change with the variation in the solvent interaction energies. High fidelity calculations using transition path sampling[55] to identify the most appropriate reaction coordinate, and rare event methods to predict the free energy barrier for kink detachment will provide accurate absolute values of the step velocity of both spiral edges.

The activity ratio of $Ca^{2+}$ to $CO_3^{2-}$ ions, $r$, is an important experimental parameter that affects the step velocity of spiral edges. Larsen et al.[51] performed *in situ* AFM experiments to measure the step velocities of the obtuse and acute spiral edges on a $(10\bar{1}4)$ surface of calcite at different values of $r$, while keeping the supersaturation constant at $S = 2.00$. We expect 2D nucleation to be important at this supersaturation value, therefore, our model predictions cannot be compared with their experiments. Stack and Grantham[43] carried out similar measurements at lower supersaturation ($S = 1.58$; Appendix B provides expressions that relate the experimental measure of supersaturation to the value of $S$ used in this article). Figure 9 shows the observed variation in the shape of the growth spirals on the calcite surface on increasing $r$.[43] The edges of the growth spiral get significantly roughened at very low or very high values of the activity ratio while the growth spiral looks more symmetric at $r \sim 1$. At very high or very low values of the activity ratio, the growth kinetics is limited by the availability of one of the two ions in the solution. At close to stoichiometric solution composition, there are plenty of both ions in the solution and the growth is limited only by the attachment/detachment kinetics.

Figure 10 shows the comparison of the experimentally measured step velocities of both obtuse and acute edges by Stack and Grantham[43] with the model predictions at different values of $r$. The model only predicts relative step velocities and not absolute values, therefore, the model predictions were scaled with an experimental value of step velocity. For obtuse edge, the experimental step velocity value at a value of $r = 43.7$ was used, while for the acute edge, the step velocity at a value of $r = 0.015$ was used for scaling. Although the model predictions do not match

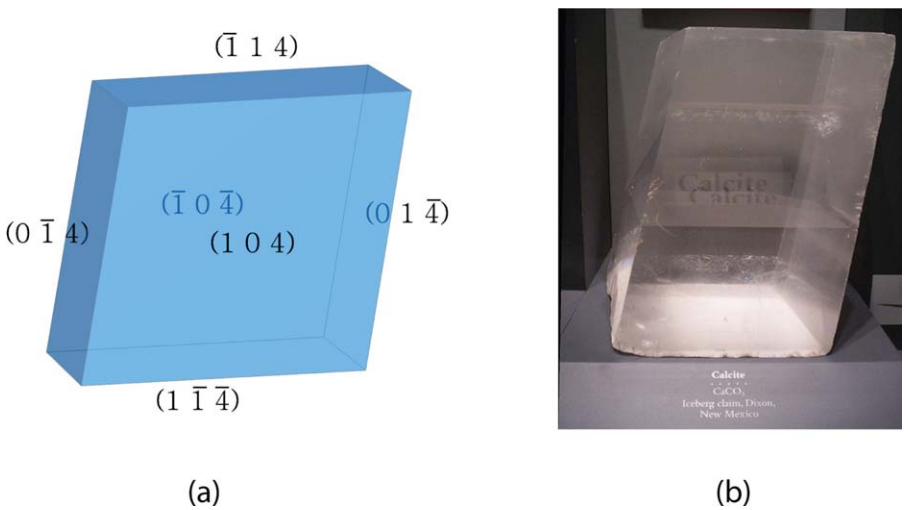


**Figure 11. (a) The predicted morphology of calcite crystals dominated by the $(10\bar{1}4)$ family of faces. (b) Morphology of the Icelandic Spar calcite crystal on exhibition at the National Museum of Natural History in Washington, DC. [Color figure can be viewed in the online issue, which is available at wileyonlinelibrary.com.]**

exactly with the experimental step velocities for both edges, the model accurately captures the step velocity trend for both the edges as the ionic activity ratio is varied. The model also correctly predicts that the maximum step velocity for each of the edges does not occur exactly at $r = 1$, which is the stoichiometric composition of the solution. As the solvation behavior and attachment rates for $Ca^{2+}$ and $CO_3^{2-}$ ions are different, the maximum step velocity will not be observed at $r = 1$.

The overall dependence of experimental parameters such as supersaturation ($S$) and ionic activity ratio ($r$) is broadly captured by this mechanistic model for the case of spiral growth on the $(10\bar{1}4)$ surface of calcite crystals. The model shows a more complex relationship between step velocity $v$ and the driving force ($S - 1$) than the simple linear relationship that was assumed by traditional models[20,56] and shown experimentally for large protein molecules.[57,58] This complex dependence on $S$ is consistent with the model developed by Zhang and Nancollas for an edge on an ionic crystal surface with two types of kink sites.[15] The scaling of the step velocity with the ionic activity ratio $r$ is also captured by this model.

The growth rate of the $(10\bar{1}4)$ calcite crystal face can be calculated by putting the values of the step velocities of the obtuse and acute edges in the $[\bar{4}41]$ and $[48\bar{1}]$ directions into Eq. 3 to calculate $\tau_s$ and the relative growth rate $G$. As there are six faces in the $\{10\bar{1}4\}$ family of F faces, they enclose the entire crystal resulting in a regular rhombohedron morphology (Figure 11 as observed in the Icelandic Spar calcite crystals[59]).

## Conclusions

A mechanistic growth model has been developed that can predict the relative growth rate of a crystal face and the steady-state morphology of inorganic crystals grown from solution. The model has been used to study the spiral growth mechanism which dominates the surface growth at low supersaturation. A generalized framework is developed to calculate the kink incorporation rate on every spiral edge on the face of an AB-type ionic crystal, irrespective of the number of kink sites exposed along each edge. The expressions for the attachment and detachment fluxes from the kink sites account for the effect of the solution composition and the kink detachment work on the kinetics of attachment and detachment processes.

The asymmetry in the step velocities on the obtuse and acute spiral edges on the $(10\bar{1}4)$ surface of calcite crystals is captured by the model. The difference in the electronic properties of the carbonate ions situated on these edges results in different kinetics of attachment and detachment from the kink sites along the edge, which is reflected in the kink detachment work ($\Delta W$) values calculated for the obtuse and acute edges. The model captures accurately the variation of the step velocity with supersaturation. The predictions match closely with the experimentally measured step velocities for the obtuse edge.[52] The ratio of the activities of $Ca^{2+}$ to $CO_3^{2-}$ ions is also an important experimental parameter with profound effect on the kinetics of step advancement of the spiral edges on calcite $(10\bar{1}4)$ surface. The model predicts the scaling of the step velocity with the activity ratio and the deviation in the maxima for the step velocities of both obtuse and acute spiral edges from the stoichiometric solution composition. The model is well suited to calculate relative step velocities of the spiral edges that can be used to predict the relative growth rates and the steady-state morphology of inorganic crystals.

The interaction energies of the surface ions with solvent (water) significantly impact the growth kinetics of inorganic crystal surfaces. This necessitates use of molecular simulations or experiments that can accurately characterize the local solvent structure and density around kink sites present on inorganic crystal surfaces. Molecular simulations coupled with rare event methods such as transition path sampling[55] and metadynamics[60] are being used to map out the free energy landscape and to calculate the absolute rates of attachment and detachment from kink sites on inorganic crystal surfaces.[49] These advances can be used to identify the exact rate determining step among the several steps involved in the growth process on inorganic crystal surfaces and to refine the kinetic expressions used in the mechanistic growth models to make them more accurate.

## Acknowledgments

We are grateful for the financial support provided by the Dow Chemical Company for endowing a doctoral fellowship awarded to P.D. and by the National Science Foundation through CBET-1159746 (M.F.D.).

## Literature Cited

1. Dandekar P, Doherty MF. A mechanistic growth model for inorganic crystals: solid state interactions. *AIChE J*. In press.
2. Haynes WM, editor. *CRC Handbook of Chemistry and Physics*. Boca Raton, FL: CRC Press, 2013.
3. Burgess J. Metal Ions in Solution. Chichester, UK: Ellis Horwood, 1986.
4. Rosseinsky DR. Electrode potentials and hydration energies. Theories and correlations. *Chem Rev*. 1965;65:467–490.
5. Gratz AJ, Manne S, Hansma PK. Atomic force microscopy of atomic-scale ledges and etch pits formed during dissolution of quartz. *Science*. 1991;251:1343–1346.
6. Gratz A, Hillner P, Hansma P. Step dynamics and spiral growth on calcite. *Geochim Cosmochim Acta*. 1993;57:491–495.
7. De Yoreo JJ, Land TA, Dair B. Growth Morphology of Vicinal Hillocks on the {101} Face of $KH_2PO_4$: From Step-Flow to Layer-by-Layer Growth. *Phys Rev Lett*. 1994;73:838–841.
8. Teng HH, Dove PM, Orme CA, De Yoreo JJ. Thermodynamics of calcite growth: baseline for understanding biomineral formation. *Science*. 1998;282:724–727.
9. Pina CM, Becker U, Risthaus P, Bosbach D, Putnis A. Molecular-scale mechanisms of crystal growth in barite. *Nature*. 1998;395:483–486.
10. Venables JA. Atomic processes in crystal growth. *Surf Sci*. 1994; 299/300:798–817.
11. Hartman P. Crystal Growth: an Introduction (North-Holland Series in Crystal Growth). North-Holland Publishing Co., Amsterdam, 1973.
12. Parker SC, Titiloye JO, Watson GW. Molecular modelling of carbonate minerals: studies of growth and morphology. *Phil Trans R Soc A*. 1993;344:37–48.
13. Soltzberg LJ, Carneiro O, Joseph GS, Khan Z, Meretsky TD, Ng MM, Ofek SA. Prediction of early- and late-growth morphologies of ionic crystals. *Acta Crystallogr B*. 1998;54:384–390.
14. Schmidt C, Ulrich J. Crystal habit prediction—including the liquid as well as the solid side. *Cryst Res Technol*. 2012;47(6):597–602.
15. Zhang J, Nancollas GH. Kink density and rate of step movement during growth and dissolution of an AB crystal in a nonstoichiometric solution. *J Colloid Interface Sci*. 1998;200:131–145.
16. DePaolo DJ. Surface kinetic model for isotopic and trace element fractionation during precipitation of calcite from aqueous solutions. *Geochim Cosmochim Acta*. 2011;75:1039–1056.
17. Diebold U, Li SC, Schmid M. Oxide surface science. *Annu Rev Phys Chem*. 2010;61:129–148.

18. Goniakowski J, Finocchi F, Noguera C. Polarity of oxide surfaces and nanostructures. *Rep Prog Phys*. 2008;71:016501.
19. Frenkel J. On the surface motion of particles in crystals and the natural roughness of crystalline faces. *J Phys USSR*. 1945;9:392–398.
20. Burton WK, Cabrera N, Frank FC. The growth of crystals and the equilibrium structure of their surfaces. *Phil Trans Roy Soc A*. 1951; 243:299–358.
21. Morse JW, Arvidson RS, Lüttge A. Calcium carbonate formation and dissolution. *Chem Rev*. 2007;107:342–381.
22. Davis KJ, Dove PM, De Yoreo JJ. The role of $Mg^{2+}$ as an impurity in calcite growth. *Science*. 2000;290(5494):1134–1137.
23. Fu G, Qiu SR, Orme CA, Morse DE, De Yoreo JJ. Acceleration of calcite kinetics by abalone nacre proteins. *Adv Mater*. 2005;17: 2678–2683.
24. Elhadj S, De Yoreo JJ, Hoyer JR, Dove PM. Role of molecular charge and hydrophilicity in regulating the kinetics of crystal growth. *Proc Natl Acad Sci USA*. 2006;103:19237–19242.
25. Stephenson AE, De Yoreo JJ, Wu L, Wu KJ, Hoyer J, Dove PM. Peptides enhance magnesium signature in calcite: insights into origins of vital effects. *Science*. 2008;322:724–727.
26. Bracco JN, Grantham MC, Stack AG. Calcite growth rates as a function of aqueous calcium-to-carbonate ratio, saturation index, and inhibitor concentration: insight into the mechanism of reaction and poisoning by strontium. *Cryst Growth Des*. 2012;12:3540–3548.
27. Bonilla G, Diaz I, Tsapatsis M, Jeong HK, Lee Y, Vlachos DG. Zeolite (MFI) crystal morphology control using organic structure-directing agents. *Chem Mater*. 2004;16:5697–5705.
28. Davis TM, Drews TO, Ramanan H, He C, Dong J, Schnablegger H, Katsoulakis MA, Kokkoli E, McCormick AV, Penn RL, Tsapatsis M. Mechanistic principles of nanoparticle evolution to zeolite crystals. *Nat Mater*. 2006;5:400–408.
29. Brent R, Lobo AJW, Lewis DW, Anderson MW. Modifying the crystal habit of zeolite L by addition of an organic space filler. *J Phys Chem C*. 2010;114:18240–18246.
30. Lupulescu AI, Kumar M, Rimer JD. A facile strategy to design zeolite L crystals with tunable morphology and surface architecture. *J Am Chem Soc*. 2013;135:6608–6617.
31. Lovette MA, Browning AR, Griffin DW, Sizemore JP, Snyder RC, Doherty MF. Crystal shape engineering. *Ind Eng Chem Res*. 2008; 47:9812–9833.
32. Dandekar P, Kuvadia ZB, Doherty MF. Engineering crystal morphology. *Annu Rev Mater Res*. 2013;43:359–386.
33. Snyder RC, Doherty MF. Predicting crystal growth by spiral motion. *Proc R Soc A*. 2009;465:1145–1171.
34. Kuvadia ZB, Doherty MF. Spiral growth model for faceted crystals of non-centrosymmetric organic molecules grown from solution. *Cryst Growth Des*. 2011;11:2780–2802.
35. Sizemore JP, Doherty MF. A stochastic model for the critical length of a spiral edge. *J Cryst Growth*. 2010;312:785–792.
36. Wolthers M, Di Tommaso D, Du Z, de Leeuw NH. Calcite surface structure and reactivity: molecular dynamics simulations and macroscopic surface modelling of the calcite-water interface. *Phys Chem Chem Phys*. 2012;14:15145–15157.
37. Zhang J, Nancollas G. Kink densities along a crystal surface step at low temperatures and under nonequilibrium conditions. *J Cryst Growth*. 1990;106:181–190.
38. Markov IV. Crystal Growth for Beginners, Fundamentals of Nucleation, Crystal Growth and Epitaxy. Singapore: World Scientific, 2003.
39. Kim SH, Dandekar P, Lovette MA, Doherty MF. Kink rate model for the general case of organic molecular crystals. *Cryst Growth Des*. 2014;14:2460–2467.
40. Eyring H. The activated complex in chemical reactions. *J Chem Phys*. 1935;3:107–115.
41. Nielsen AE. Theory of electrolyte crystal growth: the parabolic rate law. *Pure Appl Chem*. 1981;53:2025–2039.
42. Mullin J. Crystallization. Oxford, UK: Butterworth-Heinemann, 2001.
43. Stack AG, Grantham MC. Growth rate of calcite steps as a function of aqueous calcium-to-carbonate ratio: independent attachment and detachment of calcium and carbonate ions. *Cryst Growth Des*. 2010; 10:1409–1413.
44. Teng HH, Dove PM, De Yoreo JJ. Kinetics of calcite growth: surface processes and relationships to macroscopic rate laws. *Geochim Cosmochim Acta*. 2000;64:2255–2266.
45. Visscher AD, Vanderdeelen J. IUPAC-NIST solubility data series. 95. Alkaline earth carbonates in aqueous systems. Part 2. Ca. *J Phys Chem Ref Data*. 2012;41:023105.
46. Davies CW. Ion Association. Butterworths, London, UK, 1962.
47. Kerisit S, Parker SC. Free energy of adsorption of water and metal ions on the $\{10\bar{1}4\}$ calcite surface. *J Am Chem Soc*. 2004;126: 10152–10161.
48. Vchirawongkwin V, Kritayakornupong C, Tongraar A, Rode BM. Symmetry breaking and hydration structure of carbonate and nitrate in aqueous solutions: a study by ab initio quantum mechanical charge field molecular dynamics. *J Phys Chem B*. 2011;115:12527–12536.
49. Stack AG, Raiteri P, Gale JD. Accurate rates of the complex mechanisms for growth and dissolution of minerals using a combination of rare-event theories. *J Am Chem Soc*. 2012;134:11–14.
50. Liang Y, Baer DR, McCoy JM, LaFemina JP. Interplay between step velocity and morphology during the dissolution of $CaCO_3$ surface. *J Vac Sci Technol A*. 1996;14:1368–1375.
51. Larsen K, Bechgaard K, Stipp SLS. The effect of the $Ca^{2+}$ to $CO_3^{2-}$ activity ratio on spiral growth at the calcite $\{10\bar{1}4\}$ surface. *Geochom Cosmochim Acta*. 2010;74:2099–2109.
52. Teng HH, Dove PM, De Yoreo JJ. Reversed calcite morphologies induced by microscopic growth kinetics: insight into biomineralization. *Geochim Cosmochim Acta*. 1999;63:2507–2512.
53. Voronkov VV, Rashkovich LN. Influence of a mobile adsorbed impurity on the motion of steps. *Sov Phys Cryst*. 1992;37:289–295.
54. Davis KJ, Dove PM, Wasylenki LE, De Yoreo JJ. Morphological consequences of differential $Mg^{2+}$ incorporation at structurally distinct steps on calcite. *Am Mineral*. 2004;89:714–720.
55. Peters B. Recent advances in transition path sampling: accurate reaction coordinates, likelihood maximisation and diffusive barrier-crossing dynamics. *Mol Simul*. 2010;36:1265–1281.
56. Chernov A, Givargizov E. Modern crystallography: crystal growth. In; Springer Series in Solid-State Sciences. Berlin: Springer-Verlag, 1984.
57. Petsev DN, Chen K, Gliko O, Vekilov PG. Diffusion-limited kinetics of the solution-solid phase transition of molecular substances. *Proc Natl Acad Sci USA*. 2003;100:792–796.
58. Vekilov PG. What determines the rate of growth of crystals from solution? *Cryst Growth Des*. 2007;7:2796–2810.
59. Large crystal of Icelandic Spar (Calcite) on display at the National Museum of Natural History Washington, DC. 2005. Available at: https://upload.wikimedia.org/wikipedia/commons/3/37/Calcite-HUGE.jpg.
60. Laio A, Parrinello M. Escaping free-energy minima. *Proc Natl Acad Sci USA*. 2002;99:12562–12566.
61. Chernov A, Petrova E, Rashkovich L. Dependence of the CaOx and MgOx growth rate on solution stoichiometry. Non-Kossel crystal growth. *J Cryst Growth*. 2006;289:245–254.
62. Langmuir D. The geochemistry of some carbonate ground waters in central Pennsylvania. *Geochim Cosmochim Acta*. 1971;35:1023–1045.

## Appendix A: Detailed Expression for the Kink Rate

The mole fractions of A and B species in a supersaturated solution are written as a function of the local solubility product $K'_{sp}$ from Eqs. 15 and 19 as

$$x_A = \frac{S\sqrt{r}}{\gamma_A}\left(\frac{\sqrt{K'_{sp}}}{M}\right) \quad x_B = \frac{S}{\gamma_B\sqrt{r}}\left(\frac{\sqrt{K'_{sp}}}{M}\right) \tag{A1}$$

The attachment and detachment fluxes on the kink sites from a supersaturated solution are written from Eqs. 10 and 11 as follows

$$j_A^+ = \frac{Sx_{eq}\sqrt{r}}{\gamma_A}\nu_A \exp\left(-\frac{\Delta U_A}{k_B T}\right) \quad j_B^+ = \frac{Sx_{eq}}{\gamma_B\sqrt{r}}\nu_B \exp\left(-\frac{\Delta U_B}{k_B T}\right) \tag{A2}$$

$$j_{2k-1}^{-}=(1-Sx')v_A\exp\left(-\frac{\Delta U_A+\Delta W_{2k-1}}{k_BT}\right)$$
$$j_{2k}^{-}=(1-Sx')v_B\exp\left(-\frac{\Delta U_B+\Delta W_{2k}}{k_BT}\right) \quad \text{(A3)}$$

where

$$Sx'=Sx_{eq}\left(\frac{\sqrt{r}}{\gamma_A}+\frac{1}{\gamma_B\sqrt{r}}\right)+x_I+x_{III} \quad x_{eq}=\left(\frac{\sqrt{K'_{sp}}}{M}\right) \quad \text{(A4)}$$

The kink rate is calculated from Eq. 9 as

$$u=\frac{x_{eq}^{2N}(S^{2N}-1)}{\sum_{\ell=1}^{N}\left\{(1-Sx')^{2\ell-2}(Sx_{eq})^{2N-2\ell}\left[(1-Sx')(O_\ell+\xi P_\ell)+(Sx_{eq})\left(\sqrt{\frac{r\gamma_B}{\gamma_A}}Y_\ell+\sqrt{\frac{\gamma_A}{r\gamma_B}}\xi Z_\ell\right)\right]\right\}} \quad \text{(A5)}$$

where

$$O_\ell=\sum_{k=1}^{N}\left\{\exp\left(-\sum_{m=0}^{2\ell-2}\frac{\Delta W_{2k+m-1}}{k_BT}\right)\right\}$$

$$P_\ell=\sum_{k=1}^{N}\left\{\exp\left(-\sum_{m=0}^{2\ell-2}\frac{\Delta W_{2k+m}}{k_BT}\right)\right\}$$

$$Y_\ell=\sum_{k=1}^{N}\left\{\exp\left(-\sum_{m=0}^{2\ell-3}\frac{\Delta W_{2k+m-1}}{k_BT}\right)\right\}$$

$$Z_\ell=\sum_{k=1}^{N}\left\{\exp\left(-\sum_{m=0}^{2\ell-3}\frac{\Delta W_{2k+m}}{k_BT}\right)\right\}$$

$$Y_1=N \quad Z_1=N$$

$$\xi=\frac{v_A}{v_B}\exp\left(-\frac{\Delta U_A-\Delta U_B}{k_BT}\right)$$

The solubility of inorganic crystals in water is often extremely low ($x_{eq} \ll 1$) so that the term $(1-Sx')$ may be approximated as $(1-x_I-x_{III})$. From Eq. A5, the leading order term for the kink rate, and therefore the step velocity, scales linearly with the concentration driving force $(S-1)$. Also, the kink rate scales as $(r^{1/2}+r^{-1/2})^{-1}$ with the ionic activity ratio $r$. Both these scalings are consistent with those reported in the lierature.[15,61] Equation A5 is used to calculate the kink rate to within a multiplicative factor $v_A\exp(-\Delta U_A/k_BT)$ that is constant everywhere on the crystal surface and will therefore drop out of the relative growth rate expressions.

$\xi$ is the ratio of the kink attachment rate constants of the cation to the anion. If the cation and anion are of similar sizes, $\xi$ can be assumed to be $\mathcal{O}(1)$ and will not affect the scaling of other quantities in Eq. A5. The value of $\xi$ for calcite growth was calculated from the estimates of the rate constants from fitting to the step velocity measurement data as reported by Bracco et al.[26] The value of $\xi$ was calculated as 0.19 for the obtuse spiral edge and 1.36 for the acute spiral edge on the $(10\bar{1}4)$ calcite surface. Although the value of $\xi$ is not constant across the two spiral edges, they are both close to $\mathcal{O}(1)$ in magnitude, and are relatively insignificant in determining the kink rate. Molecular simulations along with rare event methods can provide accurate values of the individual attachment rate constants for both ions, and therefore of $\xi$.

The kink rate expression for the spiral edges on the $(10\bar{1}4)$ surface of calcite can be written by putting $N=2$ into Eq. A5 as follows

$$u=\frac{x_{eq}^4(S^4-1)}{b_1S^3+b_2S^2+b_3S+b_4} \quad \text{(A6)}$$

where $b_i$ are coefficients that depend on $r$, $\xi$, $\Delta W$, $x_{eq}$ and so forth.($i=1, 2, 3, 4$). This expression for the kink rate can be simplified in a Taylor series in powers of $(S-1)$ expanded around $S=1$. For the obtuse and acute edges on the $(10\bar{1}4)$ surface of calcite, the expansion for the kink rate (at $r=1.04$) is as follows

$$u_{obtuse}=33.73(S-1)+7.53(S-1)^2+7.39(S-1)^3+5.9(S-1)^4+\ldots \quad \text{(A7)}$$

$$u_{acute}=5.31(S-1)-0.42(S-1)^2+1.45(S-1)^3-0.91(S-1)^4+\ldots \quad \text{(A8)}$$

Equations A7 and A8 show that the kink rate, and therefore, the step velocity of calcite spiral edges has a nonlinear dependence on the concentration driving force $(S-1)$. This nonlinear dependence on $(S-1)$ is different from the classical crystal growth models[20,56] that assumed that the step velocity is linearly dependent on $(S-1)$.

## Appendix B: Relationships Between Various Measures of Supersaturation

We have used $S$ (from Eq. 13) to quantify a supersaturated solution in this article. A supersaturated solution is also quantified by the saturation index (SI) in geochemistry literature.[62] In solution growth literature,[35,42] the level of supersaturation is often written as $\sigma=\frac{C}{C_{eq}}-1$, where $C$ and $C_{eq}$ are the solute concentrations in the supersaturated and saturated solutions, respectively. The relationship between $S$, $\sigma$, and SI for an AB type electrolyte is

$$\sigma=S-1=\left(\frac{a_Aa_B}{K_{sp}}\right)^{1/2}-1 \quad \text{(B1)}$$

$$SI=\log\left(\frac{a_Aa_B}{K_{sp}}\right)=\log S^2=\log(1+\sigma)^2 \quad \text{(B2)}$$

*Manuscript received Mar. 14, 2014, and revision received May 19, 2014.*